J. Fluid Mech. (2011), *vol.* 669, *pp.* 584–606. © Cambridge University Press 2011
doi:10.1017/S0022112010005318

Flow field around a vibrating cantilever: coherent structure eduction by continuous wavelet transform and proper orthogonal decomposition

Y.-H. KIM[1], C. CIERPKA[2]† AND S. T. WERELEY[3]

[1]Energy Business Department, Growth and Investment Division, POSCO, 892 Daechi 4-dong Gangnam-gu, Seoul 135-777, South Korea

[2]Institute for Fluid Dynamics and Aerodynamics, University of the Federal Arms Munich, Werner-Heisenberg-Weg 39, 85577 Neubiberg, Germany

[3]Department of Mechanical Engineering, Purdue University, West Lafayette, IN 47907-1288, USA

(Received 27 April 2010; revised 4 October 2010; accepted 4 October 2010; first published online 14 January 2011)

The velocity field around a vibrating cantilever plate was experimentally investigated using phase-locked particle image velocimetry. Experiments were performed at Reynolds numbers of $Re_h = 101,\ 126$ and 146 based on the tip amplitude and the speed of the cantilever. The averaged vector fields indicate a pseudo-jet flow, which is dominated by vortical structures. These vortical structures are identified and characterized using the continuous wavelet transform. Three-dimensional flow features are also clearly revealed by this technique. Furthermore, proper orthogonal decomposition was used to investigate regions of vortex production and breakdown. The results show clearly that the investigation of phase-averaged data hides several key flow features. Careful data post-processing is therefore necessary to investigate the flow around the vibrating cantilever and similar highly transient periodic flows.

Key words: shear layers, vortex dynamics, vortex shedding

1. Introduction

A fan is an airflow generation device used for ventilation, cooling or other gaseous transportation. Among the many kinds, the three most popular are: axial, centrifugal and crossflow fans. All these types of fan typically consist of multiple aerodynamically shaped blades and an electric motor to rotate the blades. They are all widely used for various applications ranging from localized cooling within small electronic devices to industrial applications that require large-scale fans. With the rapid development of manufacturing techniques in small electronics as well as the need for small-scale fluid transportation devices in bioengineering, smaller fans are needed. However, small-scale electric motors for blade rotation are difficult to manufacture because of their complex geometries. To produce fans for smaller applications, a completely different driving mechanism for the creation of an airflow is required.

Swinging a plate back and forth is a good alternative and one of the simplest flow generation methods. Flow can be generated by a plate and an actuator flapping the

The first and the second author contributed equally to the paper.

† Email address for correspondence: christian.cierpka@unibw.de

https://doi.org/10.1017/S0022112010005318 Published online by Cambridge University Press

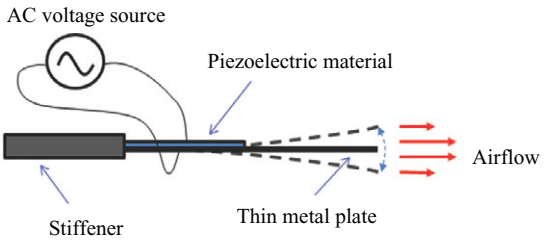


FIGURE 1. (Colour online) Schematic sketch of the working principle of the piezoelectric fan. AC, alternating current.

plate. A piezoelectric fan is one such device that generates wind using a flapping motion. As shown in figure 1, a simple piezoelectric fan is composed of a thin metal plate, clamped at one end and free at the other, onto which a piezoelectric material is deposited. The plate is deflected as a bimetallic strip when an electric potential difference is applied across the piezoelectric material, causing a deformation of the piezoelectric material proportional to the applied voltage. When an alternating-current potential is applied to the piezoelectric material, especially at the fundamental natural frequency of the cantilever, a flapping motion of the plate generates a flow.

Even this considerably simplified wind generation device has not been well described in the literature. The mechanism by which a flow is generated from a vibrating cantilever is not well understood. In addition, very little attention has been paid to understanding the flow field around a vibrating cantilever. Since the first studies on the airflow generation and heat transfer using piezoelectric fans by Toda (1979, 1981), several studies of the flow produced by a vibrating cantilever were performed using flow visualization, laser Doppler velocimetry (LDV) and numerical simulation techniques (Watanabe *et al.* 1990; Ihara & Watanabe 1994; Tsutsui *et al.* 1996; Takato *et al.* 1997). Ihara & Watanabe (1994) identified a time sequence of a pair of vortices induced by a cantilever plate during one period by means of the smoke-wire method. Two-dimensional numerical simulations using the discrete vortex method combined with the singularity method were also carried out, which showed that the tracer particle movements in the numerical simulations were in good agreement with the smoke-wire flow visualization. The numerical simulation by Takato *et al.* (1997) showed the time-averaged flow field near the plate as well as the time sequence of the velocities at several locations. However, no attention was paid to the time sequence of the vortex generation. The flow studies using LDV measurements could not show the details of the vortical flow because of low spatial resolution. Yoo, Hong & Cao (2000) used several different fan geometries and measured the resonant frequency, the tip displacement and the induced flow speed. The experimental study of the flow fields generated by a micro-scale cantilever fan by Linderman, Sett & Bright (2001) is notable because of the cantilever length of only 130 μm. Another possible application of the cantilever fan is blood pumping and chemical reagent dosage in bioengineering as shown by Lima *et al.* (2009). With the increasing interest in smaller electronics, various studies aimed at building an electric cooling fan for small-scale applications were conducted by Burmann, Raman & Garimella (2002), Acikalin, Raman & Garimella (2003), Acikalin *et al.* (2004), Wait *et al.* (2004, 2007) and Kimber & Garimella (2009), depending on various approaches – namely analytical, computational and experimental methods. In the main, flow visualizations were used to verify the results. Until Kim, Wereley & Chun (2004)

https://doi.org/10.1017/S0022112010005318 Published online by Cambridge University Press

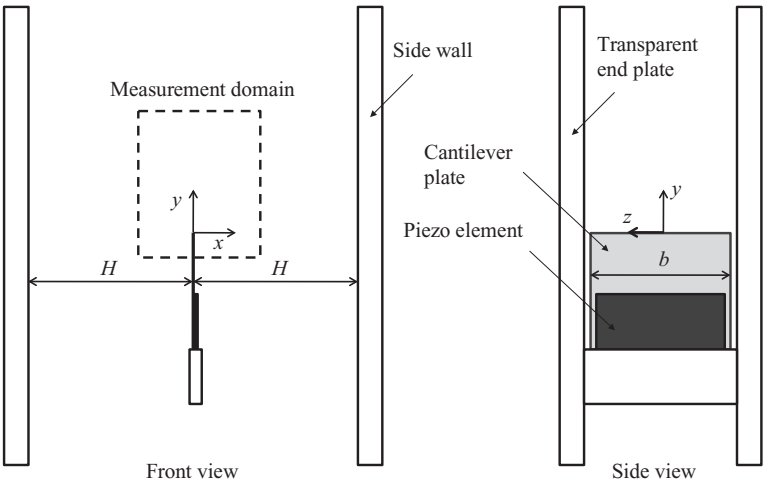


FIGURE 2. Schematic of the experimental set-up.

performed particle image velocimetry (PIV) measurements, it was not possible to identify clearly the cyclic generation of counter-rotating vortices shed from the end of a cantilever in a quantitative manner because of the low spatial resolution of the velocity previously measured using LDV. A piezoelectric fan was used as a vibrating cantilever. The vortex generation mechanisms from the end of a vibrating cantilever were clearly identified by the quantitative phase-averaged velocity fields.

In the quantitative approaches to analyse the vortex generation from a periodically vibrating cantilever, phase-averaging was typically applied to low-noise velocity field measurements, which, of course, removes the fluctuating velocity components at every phase. However, since the locations of the vortex centres are fluctuating even at the same phase, the simple phase-averaging of the fluctuating velocity fields underestimates the peak velocity and vorticity field. In order to overcome these limitations and to reveal the physical mechanisms behind the flow, in this study the vortex evolution is investigated by a wavelet-based vortex identification and the proper orthogonal decomposition (POD) method. A short introduction to the experimental set-up and the applied wavelet analysis, as well to POD, is given in § 2. Results for the fluctuating flow during one phase, the vortex evolution and the three-dimensional flow effects are discussed in § 3. A brief conclusion based on these results and an outlook for further investigations can be found in § 4.

2. Experimental set-up and post-processing

2.1. *Experimental set-up*

In the following, there will be a brief explanation of the experimental conditions. Details of the experimental techniques are provided in Kim *et al.* (2004). Figure 2 illustrates the set-up, showing a piezoelectric fan and the velocity measurement domain. The piezoelectric fan is fixed to the apparatus in a cantilevered manner with its bottom end clamped and top end free. The width of the piezoelectric fan, defined as b, is 38.1 mm. The effective length, defined as c, is 25.4 mm. It is fixed between two end plates: a transparent front wall and a rear wall. Sidewalls are placed on either side of the cantilever. The distance from the undeflected plate to either of the two sidewalls, which is represented as H, is 141 mm. Half of the peak-to-peak

https://doi.org/10.1017/S0022112010005318 Published online by Cambridge University Press

amplitude of the cantilever tip vibration is represented as h_0, and the maximum tip speed is denoted as V_T. The vibrating frequency f_0 studied here is fixed to 180 Hz, the fundamental natural frequency of the plate. The Reynolds number based on the tip vibration amplitude, Re_h, is defined as $Re_h = V_T h_0/v$.

The flow fields are studied using the PIV technique. Images are recorded using a 12 bit grey level 1280 × 1024 pixel interline transfer charge-coupled device camera and a 60 mm macro lens. A dual-cavity 120 mJ Nd:YAG laser is used to illuminate the flow. Background noise is removed by an average background removal technique. Velocity fields for eight different phases are acquired by using an external trigger. The electrical signal from the piezoelectric amplifier is used as an external trigger signal for phase-locked image acquisition.

The particles used have been generated by a studio fog machine (Rosco) and have a mean diameter of $d_P \approx 5$ μm. For these particles the buoyancy effect has been estimated following Raffel *et al.* (2007) to be of the order of <0.05 % of the tip speed V_T. Owing to inertia the particles are not able to follow the flow instantaneously. The highest acceleration can be calculated by the second derivative of the tip movement and is $\ddot{x} = h_0\omega^2 \sin(\omega t)$. The velocity lag for particles exposed to this accelerations is, according to Raffel *et al.* (2007), of the order of 8.7 % of the tip speed V_T and is expected to be much lower away from the tip, where the acceleration is much smaller.

For the current study, a multi-pass adaptive window shifting (64 × 64 ⇒ 32 × 32 pixels with 50 % overlap) and the central-difference image correction technique developed by Wereley & Gui (2003) are used to evaluate the experimental images. The peak in the correlation plane is determined with sub-pixel accuracy, and peak locking could effectively be avoided. For the applied multi-grid cross-correlation method, typically above 10 particle images with a mean diameter of $d_I \approx 2.3$ pixels are found in each interrogation window. The accuracy for the displacement estimation is for these conditions between 0.05 and 0.07 pixels (Wereley & Gui 2003). Considering the time delay to be exactly $\Delta t = 30$ μs, this results in an uncertainty of the velocity of 1.7 % of the tip speed V_T. Since all uncertainties should be independent, an overall uncertainty in the worst case of $\epsilon_u \approx 8.9$ % of the tip speed V_T close to the tip can be estimated for the measurements. Since the biggest part is due to the high acceleration of the cantilever tip, further away from the tip, where the particles follow the flow ideally, the uncertainty would be 1.7 %.

For the calculation of the derivatives a central scheme has been used. The uncertainty ϵ_ω is, according to Raffel *et al.* (2007), $\epsilon_\omega \approx 0.7\epsilon_u/\Delta X$, where $\epsilon_u = 8.9$ % of the tip speed V_T is the error of the velocity measurement and ΔX the grid spacing. For the vorticity this uncertainty doubles, since two derivatives have been used. The uncertainty of the non-dimensional vorticity $\epsilon_\omega h_0/V_T \approx 0.92$. The average vorticity in table 1 ranges from $\omega_{P,ave} h_0/V_T = 5$ to $\omega_{P,ave} h_0/V_T = 15$ which gives an uncertainty of 6.2–18.7 %. Again, a much lower uncertainty is expected in the field further away from the cantilever tip.

In total, 66 image pairs are captured for each set of experimental conditions and phase angles in this study. Flow field measurements are conducted for tip deflections of $h_0/c = 0.045, 0.050$ and 0.054 in order to observe the effects of the tip vibration amplitude. The corresponding values of the Reynolds number Re_h for these amplitudes are 101, 126 and 146, respectively. Table 2 shows the experimental parameters for the different tip amplitudes. The velocity measurement domain is 11 × 13.8 mm^2. The motion of the cantilever has been measured using a laser vibrometer (Polytec OFV511/OFV3001). The experimentally measured vibration shapes agree well with the analytical deflection shapes at the fundamental frequency, and no lateral modes

https://doi.org/10.1017/S0022112010005318 Published online by Cambridge University Press

		$\phi = 0°$	$\phi = 45°$	$\phi = 90°$	$\phi = 135°$	$\phi = 180°$	$\phi = 225°$	$\phi = 270°$	$\phi = 315°$
$\Omega_P h_0/V_T$	CCW	11.81	10.83	8.82	8.55	6.79	5.16	3.51	–
	CW	6.65	5.16	3.86	7.79	11.61	9.15	8.92	7.65
$\omega_{P,ave} h_0/V_T$	CCW	14.38	12.86	11.38	10.18	9.76	7.54	5.10	9.22
	CW	8.19	6.62	5.23	11.12	11.78	10.08	10.19	9.62
$\omega_{P,std} h_0/V_T$	CCW	1.67	1.05	1.47	1.14	1.15	1.36	1.25	3.32
	CW	0.72	0.93	0.81	3.08	1.16	0.89	0.99	0.99

TABLE 1. Vorticity at each phase of the cantilever deflection for the centre plane and $Re_h = 126$: $\Omega_P h_0/V_T$, peak vorticity at the phase-averaged flow field; $\omega_{P,ave} h_0/V_T$, average value of the peak vorticity at each flow field; $\omega_{P,std} h_0/V_T$, standard deviation of the peak vorticity at each flow field.

Re_h	h_0/c	h_0 (mm)	V_T (m s^{-1})
101	0.045	1.14	1.29
126	0.050	1.27	1.43
146	0.054	1.37	1.54

TABLE 2. Experimental parameters.

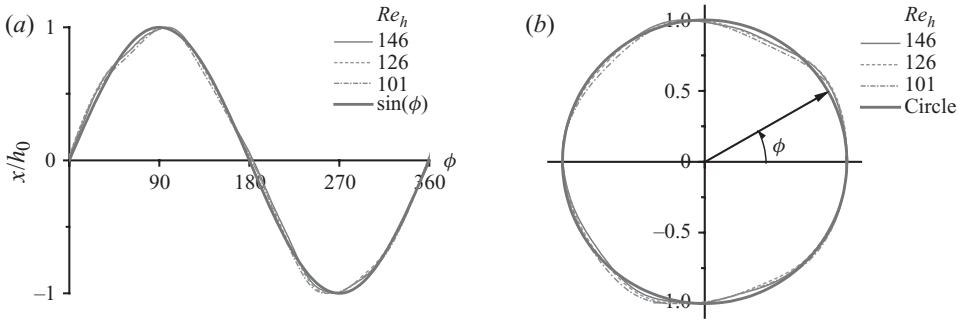


FIGURE 3. Definition of the phase angles and deflections at the centre of the cantilever tip for all Reynolds numbers (*a*) as a time series plot and (*b*) in polar coordinates.

of vibration are present (Kim *et al.* 2004). Figure 3 shows the relationship of the phase angles to the deflections of the cantilever tip. Even though slightly asymmetric deflections of the cantilever plate are observed, the motion of the tip is almost sinusoidal for all Reynolds numbers according to the time series data.

2.2. *Post-processing*

Obviously, the flow under investigation is inherently unsteady, and the mechanisms for mean flow generation from zero mean boundary motion are quite complex. The averaged velocity fields can give a first impression of the flow but will hide important features. In the previous study of Kim *et al.* (2004), flow fields induced by the vibrating cantilever were studied by primarily examining the phase-averaged velocity fields. The averaging scheme was based on the different phases of the movement of the cantilever plate, which is a good first choice, since the cantilever is the driving mechanism of the whole flow. Kim *et al.* (2004) clearly showed by the phased-averaged velocity and vorticity data that vortices are very important for the development of the flow.

https://doi.org/10.1017/S0022112010005318 Published online by Cambridge University Press

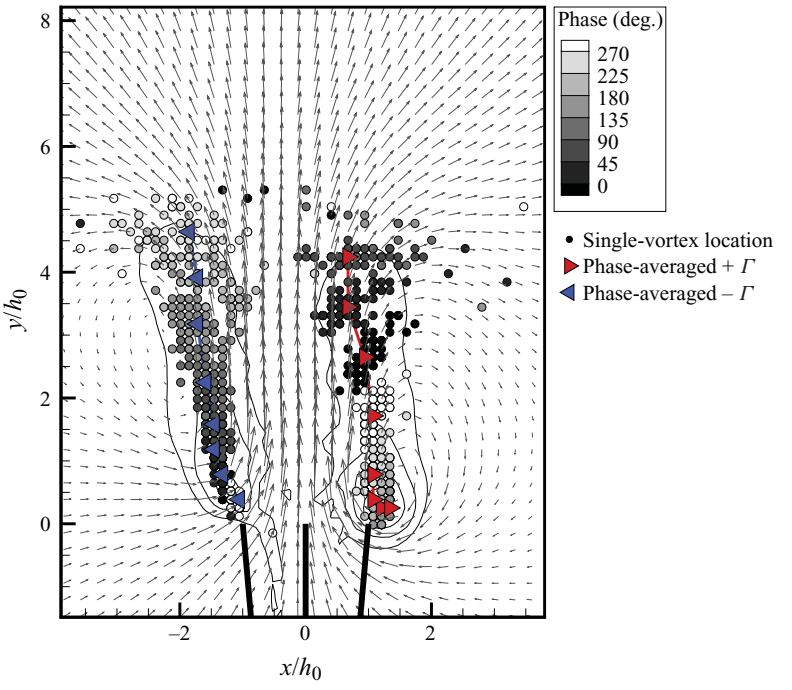


FIGURE 4. (Colour online) Averaged velocity vector field for the centre plane $z/b = 0$ for $Re_h = 146$. The lines represent the isovorticity contours. The scatter indicates the single-vortex locations (circles) and the phase-averaged vortex locations (triangles).

However, even at the same phase, the velocity field is not stationary. Locations of the vortices' centres are fluctuating as can be seen in figure 4 for a Reynolds number of $Re_h = 146$.

Phase-averaging will therefore hide features of the flow characteristics, fluctuating even at the same phase. Additionally, the peak vorticity at a vortex centre of the phase-averaged velocity fields will be 'smeared' among the samples taken at different times but the same phase and will therefore provide an underestimation of the peak vorticity and velocity compared with that observed in the individual, i.e. time-resolved vortex, measurements. Summing up, with conditional averaging one might run into the 'risk of obtaining results that are more representative of the conditional event than of the coherent structure' (Adrian 1996). Therefore, different methods are required for a detailed study of such fluctuating flows. Since the flow field generated by a vibrating cantilever can be represented quite well using counter-rotating vortices, vorticity fields are mainly used in this investigation. To extract these vortices or coherent structures from the velocity fields, several methods have been proposed and discussed in the past, e.g. by Bonnet *et al.* (1998). For the present paper the continuous wavelet transform was chosen to analyse the data and provide suitable information to characterize the vortices' behaviour. In addition, POD was applied to highlight regions of strong momentum transfer and to gain further insight into the evolution of the pseudo-jet produced by the vibrating cantilever. It is not within the scope of this paper to give a complete treatment of both approaches. Nevertheless, a brief description of both techniques is given in the following section to provide a better understanding of how they are applied to this problem.

https://doi.org/10.1017/S0022112010005318 Published online by Cambridge University Press

2.3. *Continuous wavelet transform*

An extensive review of wavelet transforms and their application to fluid dynamics was given by Farge (1992). The use of the continuous wavelet transform to identify vortical structures was introduced by Schram, Rambaud & Riethmuller (2004). The wavelet analysis is selective in space and scale and is therefore applicable for the investigation of coherent structures. A two-dimensional Marr wavelet (also known as the Mexican-hat wavelet) has been used to analyse the vorticity fields of each flow representation measured by PIV. Different vortex characteristics such as vortex size and circulation, trajectories and mean convection velocities have been determined and can be used for a better understanding of the underlying phenomena.

For some general aspects of wavelet analysis the interested reader is referred to the short introduction of wavelet analysis for data processing by Schram *et al.* (2004), although the vortex detection scheme used here differs from that used by Schram *et al.* (2004) in that the absolute value of the vorticity field is used to detect the vortices instead of the enstrophy field.

The wavelet transform of a signal $(\Psi_{l\boldsymbol{x}'}|f)$ is given by the convolution of the signal $f(\boldsymbol{x})$ and the wavelet family $\Psi_{l\boldsymbol{x}'}$:

$$\langle \Psi_{l\boldsymbol{x}'}|f\rangle = \int_{R^n} f(\boldsymbol{x})\Psi^*_{l\boldsymbol{x}'}(\boldsymbol{x})\mathrm{d}^n\boldsymbol{x}, \tag{2.1}$$

where Ψ^* denotes the complex conjugate of Ψ, $\boldsymbol{x}'$ the position and l the scale of the wavelet.

The wavelet transform was applied to the vorticity:

$$\omega_z = \frac{\partial v}{\partial x} - \frac{\partial u}{\partial y}, \tag{2.2}$$

where u and v denote the velocity components in the x-direction and the y-direction, respectively. Moreover, ω_z was obtained via a central-difference scheme (Raffel *et al.* 2007). The vorticity is generally a well-suited basis for detecting vortices, since vortices are regions of high vorticity. Furthermore, the vorticity is a Galilean invariant. Its major drawback is the appearance of high vorticity not only in regions of swirling motion, i.e. the vortices, but in regions of high shear rates as well, i.e. in the shear layer along the cantilever plate. In the flow fields studied here, both vortices and shear layers are present, and it is difficult to differentiate between them by applying a simple threshold criterion. In the study of Kim *et al.* (2004) spatial-weighting functions were used to filter the vorticity. In the present study, the λ_2-criterion, as proposed by Jeong & Hussain (1995), has been used in order to distinguish between the coherent structures and the shear layer at the cantilever plate. This criterion is based on the second highest eigenvalue λ_2 of the velocity gradient tensor. If the λ_2-criterion is satisfied, i.e. for $\lambda_2 < 0$, a vortex is expected, since the rotational part of the velocity gradient tensor is larger than the one due to deformation. In the shear layer, where the vorticity is due to deformation, λ_2 is positive. Using the λ_2-criterion as the filter function allows the extraction of the vortices from the shear layers:

$$\omega_z = \begin{cases} \omega_z & \text{if } \lambda_2 < 0, \\ 0 & \text{if } \lambda_2 \geqslant 0. \end{cases} \tag{2.3}$$

Kim *et al.* (2004) showed that the vorticity distribution of the phase-averaged vortices for this flow is very similar to the vorticity distribution of Lamb–Oseen vortices. The vortex detection algorithm can therefore be calibrated with the theoretical model of

https://doi.org/10.1017/S0022112010005318 Published online by Cambridge University Press

the Lamb–Oseen vortex defined as follows:

$$u_\phi(r) = \frac{\Gamma}{2\pi r}\left[1 - \exp\left(\frac{r^2}{2\sigma^2}\right)\right], \tag{2.4}$$

$$\omega(r) = \frac{\Gamma}{2\pi\sigma^2}\exp\left(\frac{-r^2}{2\sigma^2}\right), \tag{2.5}$$

where u_ϕ denotes the tangential velocity, Γ the circulation and σ the size of the vortex. The size of the vortex core, Dc, is usually defined by the maximum of the tangential velocity and can be determined to be $Dc = 3.17\sigma$ for the Lamb–Oseen vortex. The wavelet coefficient for a Lamb–Oseen vortex is now defined to be

$$\langle \Psi_l | \omega \rangle = 2\pi \int_0^\infty \underbrace{\frac{\Gamma}{2\pi\sigma^2}\exp\left(\frac{-r^2}{2\sigma^2}\right)}_{\omega} \underbrace{\frac{1}{l}\left(2 - \frac{r^2}{l^2}\right)\exp\left(-\frac{r^2}{2l^2}\right)}_{\Psi_l} r\,\mathrm{d}r \tag{2.6}$$

which gives after some algebra the derivative of the scale as

$$\frac{\partial \langle \Psi_l | \omega \rangle}{\partial l} = -\frac{2\Gamma l^2(l^2 - 3\sigma^2)}{(l^2 + \sigma^2)^3} \tag{2.7}$$

and therefore a maximum for $l/\sigma = \sqrt{3}$. Using this relation it is possible to associate a certain vortex core diameter with the maximum wavelet coefficient. For the details, the interested reader is referred to Cierpka, Weier & Gerbeth (2008).

It has to be mentioned that a criterion has been used to ensure that a detected structure is indeed a vortex. The absolute value of the wavelet coefficient depends on the size of a vortex and its strength. The ratio between the detected wavelet coefficient and the theoretical one, β, can be calculated on the basis of the vorticity at the centre of the structure. In the following, the β-criterion for a valid vortex is required to have at least an 80 % agreement between the Lamb–Oseen vortex model and the detected structure.

In order to have the best possible choice for the wavelet scales l, the algorithm calculates the size of possible structures in advance by calculating an equivalent diameter of connected regions of negative λ_2. The range for the wavelet scales is then adjusted to cover the smallest and largest equivalent diameters. This method can decrease the computational time and enhance the accuracy of the algorithm, since the range is adjusted if necessary, for situations in which the sizes of the vortices may vary. The vortices increase in size for further downstream coordinates. To ensure an accurate detection, larger wavelets, i.e. a larger-scale parameter l in (2.7), are needed. For the present study the range for the wavelet scales has been set to 200 discrete l and is updated for every vector field processed. The final procedure is now to read a vector field, calculate the vorticity and apply the λ_2-filter. The estimation of the size of possible structures gives the range of wavelet scales. According to this, the wavelets are then calculated. The practical implementation of the convolution in (2.1) has been done using a two-dimensional fast Fourier transform of the vorticity field and the wavelets. Their multiplication and a final back transformation yields the fields of wavelet coefficients for each scale. The maxima among the scales are then determined, and the reliability criterion is applied. If a structure is identified to be a vortex, certain flow variables are extracted and stored for further analysis.

https://doi.org/10.1017/S0022112010005318 Published online by Cambridge University Press

2.4. *Proper orthogonal decomposition*

POD has been applied to decompose the velocity and vorticity fields. The POD method was introduced in the field of fluid mechanics by Lumley (1967). An overview of the method and its possible applications can be found, e.g. in Berkooz, Holmes & Lumley (1993). The method has become widely used for the identification of coherent structures (Hilberg, Lazi & Fielder 1994; Bonnet *et al.* 1998; Delville *et al.* 1999) and low-order modelling of turbulent flows (Holmes *et al.* 1997; Smith, Moehlis & Holmes 2005; Bourguet & Braza 2007; Siegel *et al.* 2007). Especially in connection with PIV data the method helps to reveal characteristic flow features (Bernero & Fiedler 2000; Braud *et al.* 2004; Kostas, Soria & Chong 2005).

The basic idea is to find an approximation of the function f,

$$f(x, y, t) \approx \sum_{k=1}^{K} a_k(t)\Phi_k(x, y), \tag{2.8}$$

which is exact for $K = \infty$. The (POD) basis functions $\Phi_k(x, y)$ are chosen to be orthonormal and as good as possible for each K in a least-squares sense (Cordier & Bergmann 2003). Considering that $f(x, y, t)$ is a flow variable, measured at N_t instants of time, (2.8) results in finding basis functions that fulfil

$$\min \sum_{i=1}^{N_t} \left\| f(x, y, t_i) - \sum_{k=1}^{K} \left(f(x, y, t_i), \Phi_k(x, y)\right) \Phi_k(x, y) \right\|_2^2, \tag{2.9}$$

where $\|.\|_2$ is the L_2 norm and $(.,.)$ the inner product of two quantities. Using velocity distributions as input, the resulting POD modes $\Phi_k(x, y)$ are an optimal decomposition in terms of kinetic energy. The POD modes used in the current paper are based on both the velocity u, v and the vorticity ω_z. Taking the vorticity as input, the resulting modes are optimal in terms of enstrophy and highlight regions of strong momentum transfer in the flow (Weier, Cierpka & Gerbeth 2008). Additionally, Kostas *et al.* (2005) have shown that for some flows the convergence of vorticity-based POD modes is prior to that of velocity-based modes. By correctly ordering the measured quantities into a matrix $\boldsymbol{A}$, the problem can be solved by singular-value-decomposition routines provided in standard libraries. To decrease the numerical effort we have followed the snapshot method as proposed by Sirovich (1987). By pre-multiplying the matrix of the measurements, $\boldsymbol{A}$, with its transpose, one ends up with the eigenvalue problem

$$\boldsymbol{A}^T\boldsymbol{A}v = \lambda v, \tag{2.10}$$

where λ are the eigenvalues and v the eigenvectors of $\boldsymbol{A}^T\boldsymbol{A}$. The POD modes can be calculated using

$$\Phi_k = \frac{1}{\sqrt{\lambda_k}} \boldsymbol{A}v_k. \tag{2.11}$$

Eigenvalue routines of Matlab were used to determine the POD modes for this investigation.

3. Results

3.1. *Fluctuating flow at constant phase*

In order to investigate the highly turbulent flow structures induced by periodic actuation, a phase-averaged technique, where measurements at many different times

https://doi.org/10.1017/S0022112010005318 Published online by Cambridge University Press

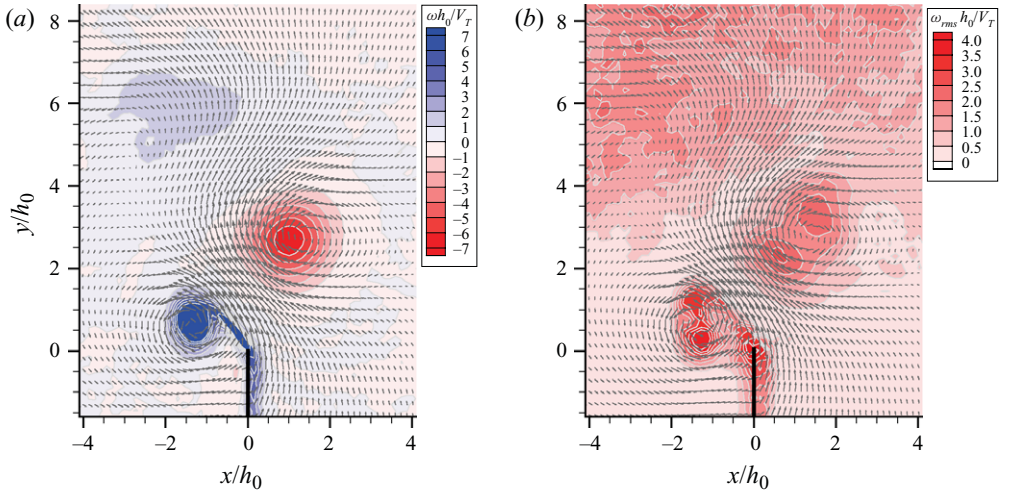


FIGURE 5. (Colour online) (*a*) Phase-averaged flow field plotted on top of average vorticity and (*b*) phase-averaged flow field plotted on top of the r.m.s. value of the vorticity fluctuation on the centre plane ($z/b = 0$) for $\phi = 0^\circ$ and $Re_h = 126$.

but at the same phase are averaged together, is surely a good first approach. The fluctuating quantities in each phase-averaged flow field which are obtained as root-mean-square (r.m.s.) values can be calculated for each phase from the measurements, but the significance of areas of high r.m.s. versus those of low r.m.s. can be difficult to determine. Especially in case of vortex-dominant flows, where each vortex is spatially scattered, even at the same driving cantilever phase, the peak vorticity in each phase-averaged flow field is underestimated, which makes the fluctuating quantities decrease rapidly, and the clear shapes of the scattered vortices coalesce into a single weak time-averaged vortex. In order to show the highly spatially fluctuating vortex flow field clearly, the wavelet analysis technique of phase-averaged flow fields is necessary, which instead indicates the distribution of vortex centre locations, as well as their sizes and magnitudes.

Figure 5 represents the phase-averaged distribution of vorticity and its r.m.s. value on the centre plane ($z/b = 0$) for $\phi = 0^\circ$ and $Re_h = 126$. The flow structure shows clearly a pair of counter-rotating vortices near the moving fan. As indicated, the r.m.s. fluctuating vorticity field is similarly shown in figure 5(*b*), but the spatially fluctuating vortices are not clearly identified.

Figure 6 shows at each phase angle the spatial distribution of the vortex core locations (circle centres) and their sizes (circle diameters) for each of the 66 instantaneous velocity fields that comprise the phase-averaged flow field for each phase angle. The birth and travel of the counter-rotating vortices near the tip as well as the breakdown of the vortices further downstream are clearly visible. While the sizes of all vortex families at each phase angle are similar in magnitude, the locations of the vortex cores are scattered, suggesting an irregular motion of the vortex structures. The principal direction of the scattered vortex centres, which is calculated by finding the straight line that fits best to all the vortex centre locations for each vortex family at each phase angle, has a strong dependence on the phase angle or, equivalently, the distance downstream of the cantilever tip. When a vortex starts to form near the cantilever tip, the principal direction is almost completely parallel to the y-axis; that

https://doi.org/10.1017/S0022112010005318 Published online by Cambridge University Press

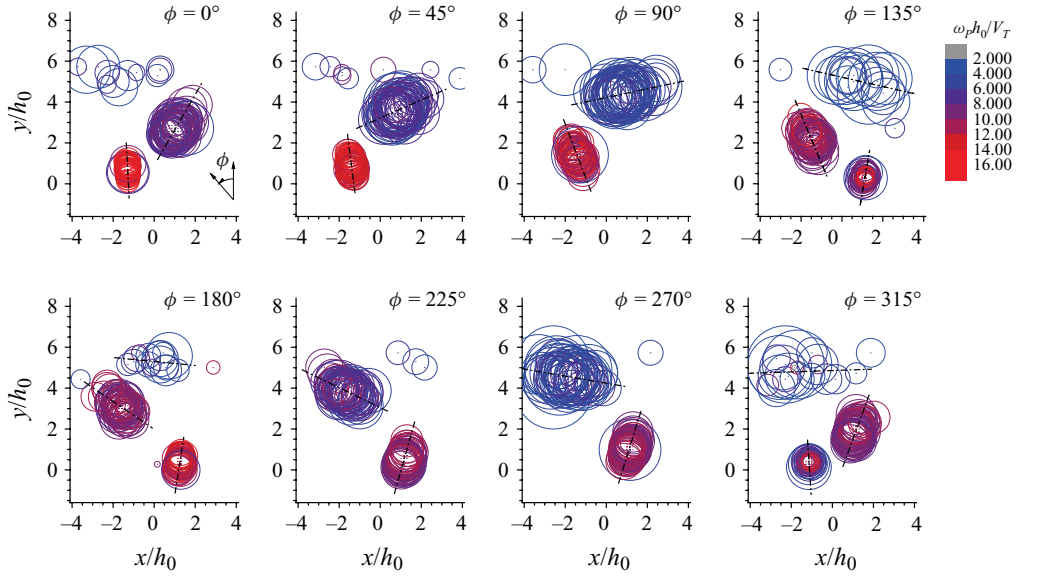


FIGURE 6. (Colour online) Spatial distribution of the vortex cores and their sizes for each of the 66 instantaneous velocity fields comprising each phase of the cantilever deflection on the centre plane for $Re_h = 126$. The circles represent the sizes and locations of each vortex core; the dash-dotted lines denote the principal direction of the vortex core scatter.

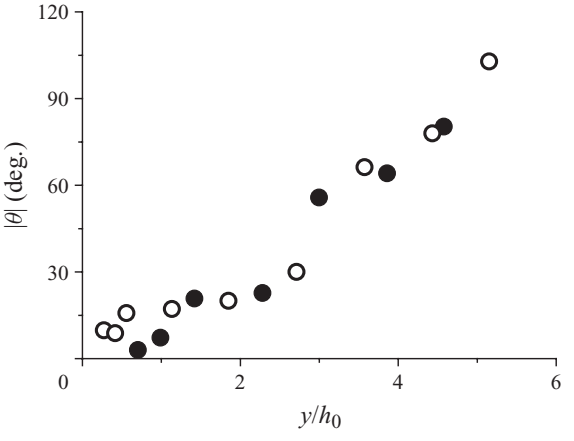


FIGURE 7. The principal direction of the vortex core scatter as a function of distance from the tip. The filled symbols represent counterclockwise vortices and the open symbols clockwise vortices. The principal direction θ is defined as shown in figure 6.

is, Θ is approximately 0°. As the vortex travels downstream, the principal direction gradually changes to become parallel to the x-axis. This variation of the principal direction is also shown graphically in figure 7. In the figure, $|\theta| = 0°$ occurs near the cantilever tip ($y/h_0 = 0$), and it increases monotonically in the downstream direction, finally reaching approximately 90° at the location of vortex breakdown, around $y/h_0 = 5$.

The other limitation of a phase-averaged flow analysis is underestimating the peak vorticity magnitude in a spatially fluctuating vortex flow. As shown in table 1 for clockwise (CW) and counterclockwise (CCW) rotating vortices, the peak vorticity

https://doi.org/10.1017/S0022112010005318 Published online by Cambridge University Press

		$\phi = 0°$	$\phi = 45°$	$\phi = 90°$	$\phi = 135°$	$\phi = 180°$	$\phi = 225°$	$\phi = 270°$	$\phi = 315°$
Dc/h_0	CCW	1.26	1.42	1.70	1.73	1.98	2.30	2.76	–
	CW	2.05	2.35	2.55	1.28	1.30	1.80	1.82	1.98
dc_{ave}/h_0	CCW	1.13	1.31	1.48	1.63	1.62	1.90	2.33	1.12
	CW	1.87	2.13	2.28	1.03	1.34	1.72	1.71	1.72
dc_{std}/h_0	CCW	0.18	0.09	0.24	0.18	0.18	0.26	0.48	0.37
	CW	0.15	0.26	0.28	0.29	0.17	0.14	0.20	0.23

TABLE 3. Vortex core size at each phase of the cantilever deflection for centre plane and $Re_h = 126$: Dc, vortex core size at the phase-averaged flow field; dc_{ave}, average value of the vortex core sizes at each flow field; dc_{std}, standard deviation of the vortex core sizes at each flow field.

extracted from the phase-averaged flow fields (Ω_P) is lower than the averaged values of the instantaneous peak vorticity ($\omega_{P,ave}$) at all phase angles. The standard deviation of the peak vorticity at each phase angle ($\omega_{P,std}$) is quite small. For instance, $\omega_{P,std}$ is only 9–11 % of $\omega_{P,ave}$ for $\phi = 0°$, while Ω_P is 81–82 % of $\omega_{P,ave}$, meaning that a two-standard-deviation 95 % confidence interval does not cover the difference between the two values. Similarly, the overestimation of vortex core size in the phase-averaged flow field can be seen in table 3. Vortex core sizes for the phase-averaged flow field (Dc) are considerably larger than the averaged value of the instantaneous vortex core sizes at each phase angle (dc_{ave}). In addition, the standard deviation of the vortex core size at each phase angle (dc_{std}) is also comparatively small. For the study of vortex-dominant flows, averaging the instantaneous vortex data is necessary for the correct identification of the shedding mechanisms and gives more reliable results than averaging of the flow fields and the later estimation of the vortex characteristics. Since the positions of the individual vortices do not coincide within the instantaneous vector fields for the same phase, their strength will be smeared according to the probability of the different locations in the individual vector fields. The averaging of instantaneous vortex data does not underestimate the strength and size of the vortices and gives statistically correct results.

As shown by these results, the individual vortex characteristics – such as the location, size and magnitude of each vortex – provide the detailed topology of spatially fluctuating vortices at each phase, which is an essential information in the study of any periodic flow.

3.2. *Vortex development in the downstream direction*

The wavelet algorithm gives the position and characteristic of every vortex in the instantaneous velocity data set. Approximately three vortices are present at any given time in the measurement region of each vector field. To study the effect of phase averaging on the trajectories of the vortices, the vortex core locations calculated from the phase-averaged flow fields were compared with the locations found by averaging each instantaneous vortex centre location over that same phase angle. Further, the instantaneous vortex core locations were compared with both of the averaged values. For the spatial averaging, the downstream coordinate y was chosen. The average y-position was obtained by sorting all available vortex data, separately for CW and CCW vortices, with increasing y-coordinate. The y-coordinate was then divided into bins having a width of 32 pixels, which corresponds to two times the grid resolution, and the mean vorticity and vortex core size of the data in a certain bin were calculated.

https://doi.org/10.1017/S0022112010005318 Published online by Cambridge University Press

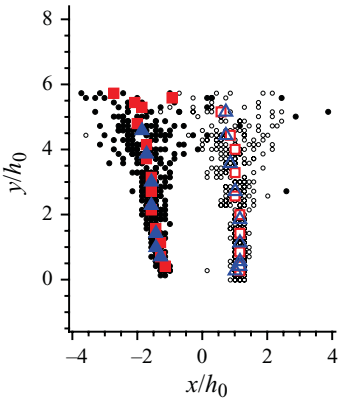


FIGURE 8. (Colour online) Trajectories of the vortex cores for the centre plane and $Re_h = 126$. The circles represent the location of each vortex core; the squares represent the averaged location of the vortex cores; and the triangles represent the location of the vortex cores of the phase-averaged flow fields. The filled symbols denote CCW vortices and the open symbols CW vortices.

As shown in figure 8, the mean trajectory of the vortex cores obtained from the phase-averaged flow fields follows well the averaged path of the vortices. Figure 9(*a*,*c*,*e*) plots the peak vorticity and and figure 9(*b*,*d*,*f*) the core size of each instantaneous vortex over the range of different Reynolds numbers tested. Clearly, the general trend is that the strength of each vortex is decreasing with increasing downstream position. In the figure, the vortex strength and size of the phase-averaged flow fields are also shown. These values also agree with the generally decreasing trend. Careful inspection of the figure reveals that the maximum vorticity in all cases occurs in the range of $0 < y/h_0 < 1$ – slightly downstream of the cantilever tip. From that point the vorticity decreases monotonically in the downstream direction, while the vortex size increases. With the increasing downstream position, the vortices break down until eventually no vortex can be detected. As discussed earlier, the vorticity in the phase-averaged flow is known to be underestimated. The more widely scattered the instantaneous vorticity values (ω_P, dc), the larger the difference between the averaged instantaneous vorticities of each vortex ($\omega_{P,ave}$, dc_{ave}) and the vorticity from the phase-averaged flow (Ω_P, Dc).

While figure 9 shows the scatter of instantaneous vortex strengths, figure 10 shows the trajectories of averaged instantaneous vortex locations for the three Reynolds numbers explored in this paper. There is a clearly observed relationship between not only the inclined vortex trajectory and the strength of the averaged vorticity ($\omega_{P,ave}$ and Ω_P) but also the inclined vortex trajectory and the strength of the degree of scattering of the instantaneous vorticity (ω_P). The trajectories of the vortex cores at $Re_h = 126$ and 146 are slightly inclined to the left ($-x$-direction). In figure 9(*c*–*f*), the strength of the averaged vorticity ($\omega_{P,ave}$ and Ω_P) of CCW vortices is seen to be greater than that of CW vortices. Moreover, the degree of scattering of the instantaneous vortex strength (ω_P) at each y/h_0 position is larger for CCW vortices for the two slightly inclined flows. Consequently, the vorticity calculated from the phase-averaged flow will considerably underestimate the vorticity as calculated from the averaged instantaneous vorticity for CCW vortices. For $Re_h = 101$, the trajectories are nearly vertical, and the degree of scatter is smaller. Further, the difference in strength between CCW and CW vortices is considerably smaller. Nonetheless, the vorticity calculated

https://doi.org/10.1017/S0022112010005318 Published online by Cambridge University Press

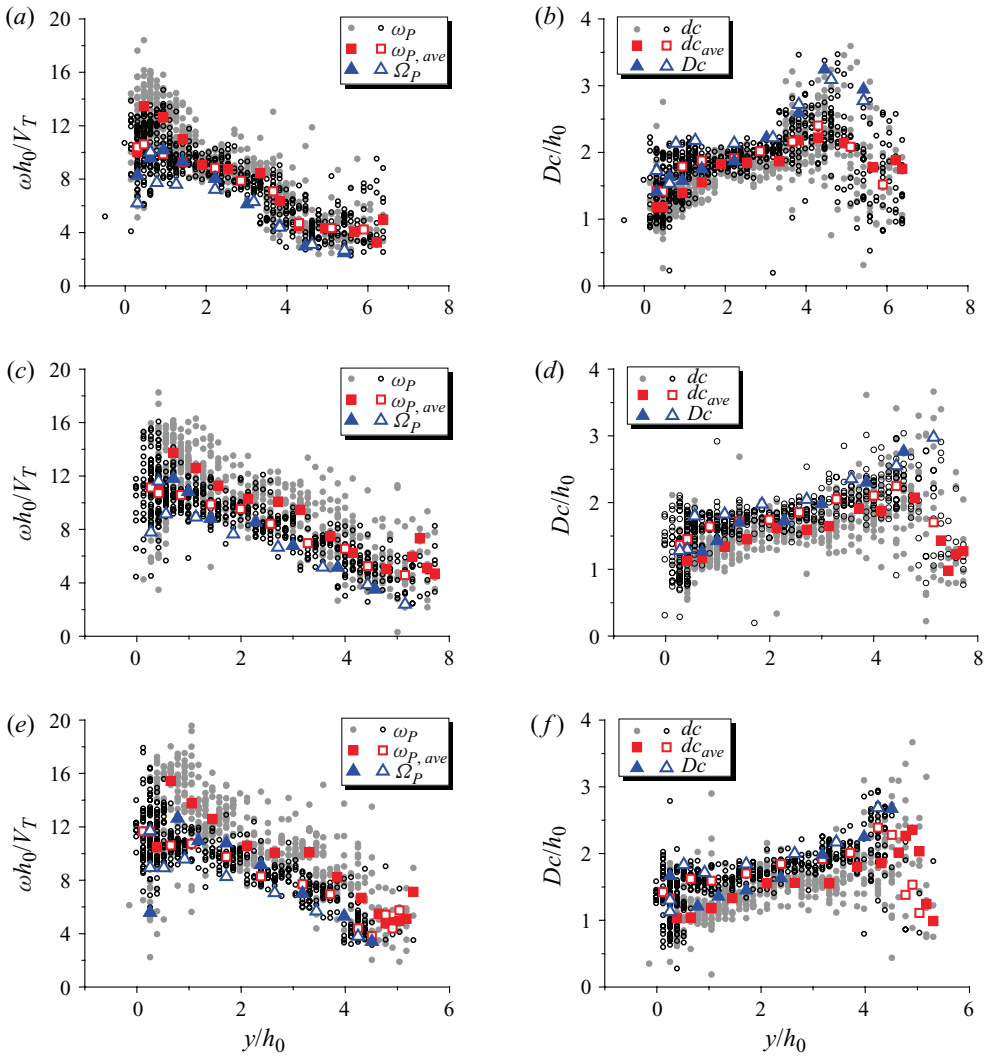


FIGURE 9. (Colour online) Growth and decay of each vortex on the centre plane: (*a*, *c*, *e*) peak vorticity; (*b*, *d*, *f*) vortex core size. The Reynolds number values are $Re_h = (a, b)$ 101, (*c*, *d*) 126 and (*e*, *f*) 146. The small circles represent the instantaneous vorticity; the squares represent averaged instantaneous vorticities; and the triangles represent vorticities of phase-averaged flow fields. The filled symbols represent CCW vortices and the open symbols CW vortices.

from the phase-averaged flow still underestimates the vorticity calculated by averaging the instantaneous vorticity.

The difference in strength between CCW and CW vortices suggests that the jet flow produced by the cantilever is asymmetric. As Kim *et al.* (2004) discussed, these asymmetric flows could be formed by a slight misalignment in the experimental apparatus or slight asymmetric deflection of the cantilever plate due to the asymmetric geometry of the cantilever itself. The piezoelectric material is attached on only one side of the thin metal plate. This asymmetric geometry causes slightly distorted harmonic motion of the cantilever tip as shown in figure 3.

https://doi.org/10.1017/S0022112010005318 Published online by Cambridge University Press

Re_h	Kinetic energy (%)	Enstrophy (%)
101	42	16
126	43	16
146	41	15

TABLE 4. Fraction of energy contributed by the mean flow to the total energy. The energy in the region of $-1.6 < y/h_0 < 8.4$ and $-4 < x/h_0 < 4$ is considered.

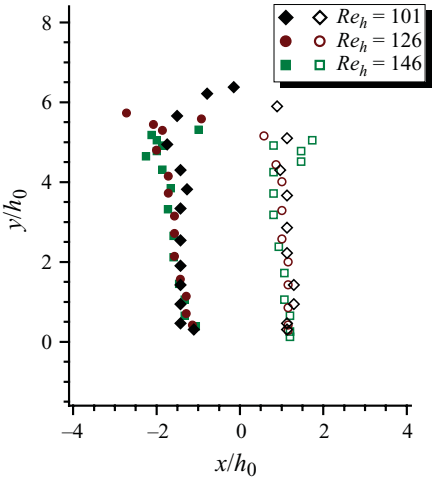


FIGURE 10. (Colour online) Trajectories of the vortex cores as calculated by averaging the instantaneous vortex centres on the centre plane for different Reynolds numbers. The filled symbols represent CCW vortices and the open symbols CW vortices.

3.3. *Mean flow fields and POD analysis*

The net effect of each vortex can be shown by averaging each flow field over a period of cantilever oscillation. The averaged flow forms a pseudo-jet with a pair of counter-rotating vortices standing just downstream of the cantilever tip. Figure 11 shows an overlaid mean velocity field for the centre plane ($z/b = 0$) for all three Reynolds numbers measured: $Re_h = 101$, 126 and 146. It may be noted that a high downstream jet is formed in between the trajectory of the phase-averaged vortex cores. The jet is collimated, seemingly confined, in the y-direction up to a distance of $y/h_0 = 4$ from the tip and spreads rapidly after $y/h_0 = 4$.

The contribution of energy in the mean flow field to the total energy contained in the flow is an indicator of the complexity of the fluctuating flow. Table 4 shows the fraction of the energy in the mean flow relative to the total energy in the fluctuating flow. Both kinetic energy and enstrophy are listed in the table in the same manner as used by Kostas *et al.* (2005) for quantifying the fluctuation in a backward-facing step. For all Reynolds numbers the mean flow contributes less than 50 % of the total flow energy. Around 60 % of the total energy is due to oscillations, indicating highly fluctuating flow. The contribution of mean enstrophy to the total flow enstrophy is much lower – only 15–16 % – suggesting that vigorous vortical motion appears in the field of investigation.

For a detailed analysis of the fluctuating flow, a POD analysis has been applied to the vector fields and the vorticity fields for the different Reynolds numbers explored. The relative contribution of each POD mode to the fluctuating enstrophy, which is

https://doi.org/10.1017/S0022112010005318 Published online by Cambridge University Press

	Velocity		Vorticity	
Mode i	$\frac{\Sigma_1^i E_i}{E_{tot}}$ (%)	$\frac{E_i}{E_{tot}}$ (%)	$\frac{\Sigma_1^i E_i}{E_{tot}}$ (%)	$\frac{E_i}{E_{tot}}$ (%)
1	19.2	19.2	19.6	19.6
2	33.0	13.9	33.3	13.7
3	34.9	1.8	37.4	4.1
4	37.4	2.5	40.5	3.2
5	40.6	3.2	43.0	2.4
6	41.1	0.5	45.2	2.2
7	41.8	0.7	46.9	1.7
8	43.7	2.0	48.5	1.6
9	44.8	1.0	49.8	1.4
10	45.7	0.9	51.0	1.2

TABLE 5. Cumulative and modewise contributions to the total enstrophy at the centre plane at $Re_h = 126$.

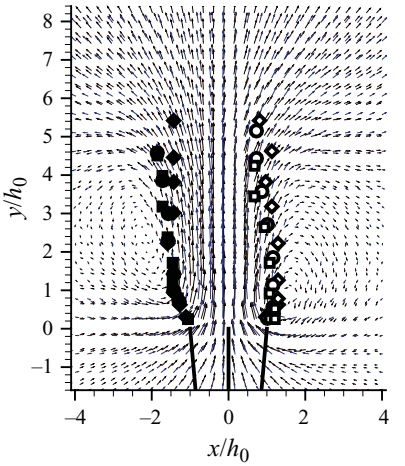


FIGURE 11. Superposition of the mean velocity fields at the centre plane of $z/b = 0$ with averaged vortex locations. The diamonds represent $Re_h = 101$, the circles $Re_h = 126$ and the squares $Re_h = 146$.

the total enstrophy minus the mean flow enstrophy, is reflected in the the eigenvalues for the vorticity-based modes. The modes of the velocity fields are optimal in energy, and the eigenvalues reflect the modal contribution of the fluctuating energy. To make a comparison on the same basis between the modes by both approaches, the corresponding vorticity field was obtained by the reconstructed velocity modes. The enstrophy related to each velocity mode can now be calculated from this corresponding vorticity field (Kostas *et al.* 2005). The normalized fraction of the enstrophy content and the cumulative fraction of the enstrophy content by each mode for both approaches are listed in table 5 for the first 10 modes. The enstrophy content of mode i is denoted by E_i; the total sum for mode 1 to i is denoted by $\Sigma_1^i E_i$; and the total sum for all modes is denoted by E_{tot}. It is observed that the most significant amount of the fluctuating enstrophy is contained in the first two modes; the enstrophy decreases rapidly with the increasing mode number. Starting from mode 3, the vorticity-based modes seem to occur pairwise with an almost equal enstrophy

https://doi.org/10.1017/S0022112010005318 Published online by Cambridge University Press

content. The total contribution of the first 10 velocity modes to the enstrophy is 46 % and is lower than for the vorticity-based modes by 51 %.

Since the content of fluctuating enstrophy is very high, by 85 % according to table 4, and since the vorticity modes represent vortex-dominant flow structures better than the velocity modes (Kostas *et al.* 2005), in figures 12 and 13 the spatial distribution of the first four vorticity modes Mw1-4 are presented together with the mean vorticity and the mean flow vectors for all three Reynolds numbers considered. The POD modes of periodic flow phenomena often occur pairwise (Siegel *et al.* 2007; Tinney & Jordan 2008). The spatial distribution of modes 1 and 2, as well as that of modes 3 and 4, indicates a relation among them.

As the first mode contains the highest enstrophy, it is likely to represent the place where the vortices are at the highest energy. In the region close to the cantilever tip the momentum transfer from the quiescent surrounding fluid to the pseudo-jet flow is at its highest value. This is found near the cantilever tip at around $y/h_0 = 0.7$ for the left side and $y/h_0 = 0.4$ for the right side. The location of high values in the first mode is in good agreement with the position at which the maximum vorticity is found as shown in figure 9. At this position the evolving vortices are shed from the shear layer on the cantilever plate and start to move further downstream. The wavelength in space of mode 1 is approximately 5 in the y/h_0-direction. It may be observed that this wavelength is almost the same as the distance between the CCW vortex near the tip and that of the previous cycle at $\phi = 0°$, located at the left side where $x/h_0 < 0$, as shown in figure 6. The first mode shows a symmetric pattern along the line of $x/h_0 = 0$, while the mean flow shows two counter-rotating flows having skew-symmetric vortices.

The mean flow affected by this mode may have alternative vortex flow patterns similar to a phase-averaged flow at $\phi = 0°$ as shown figure 5. The positive values near $(x/h_0,\ y/h_0) = (-1.3,\ 0.7)$ in the first mode and the negative ones near $(x/h_0,\ y/h_0) = (1.3,\ 3.0)$ make the vorticity in the mean flow stronger, while the negative values near $(x/h_0,\ y/h_0) = (-1.7,\ 3.3)$ and the positive ones near $(x/h_0,\ y/h_0) = (1.3,\ 0.4)$ make the vorticity in the mean flow weaker. For the second mode, the position of high momentum transfer is shifted roughly one quarter wavelength in space in the downstream direction and represents the entrainment of fluid due to the downstream motion of the vortices. Nevertheless regions of high momentum exchange occur close to the tip of the cantilever and even in between the positions of the fully deflected cantilever. This indicates that the direct movement of the cantilever also produces vorticity and contributes to the mean flow for $y/h_0 < 0$. This feature first occurs in the the second mode, which contributes by 13 % to the total enstrophy compared with 20 % of mode 1. The more dominant process to feed the pseudo-jet is therefore the shedding of the vortices at the cantilever tip as indicated in mode 1. Similar to the first mode, the wavelength, in the y/h_0-direction, of the second mode is almost the same as the distance between the CCW vortex near the tip and that of the previous cycle at $\phi = 315°$. The third and fourth modes occur pairwise with approximately the same contribution to the total enstrophy ($\sim$4 %). Such a pairwise occurrence of POD modes is typical for bluff body wakes, even for the first modes. Since this is not the case here, the phenomenon related to active vortex generation due to the moving cantilever plate differs significantly from a wake flow with passive vortex shedding. Additionally, modes 3 and 4 are much weaker than modes 1 and 2. However, the wavelength is half of those for the first and second modes. In case of $Re_h = 101$, which has a symmetric mean flow as shown in figure 13(*d*,*e*), the mode shape shows a skew-symmetric pattern along the line of

https://doi.org/10.1017/S0022112010005318 Published online by Cambridge University Press

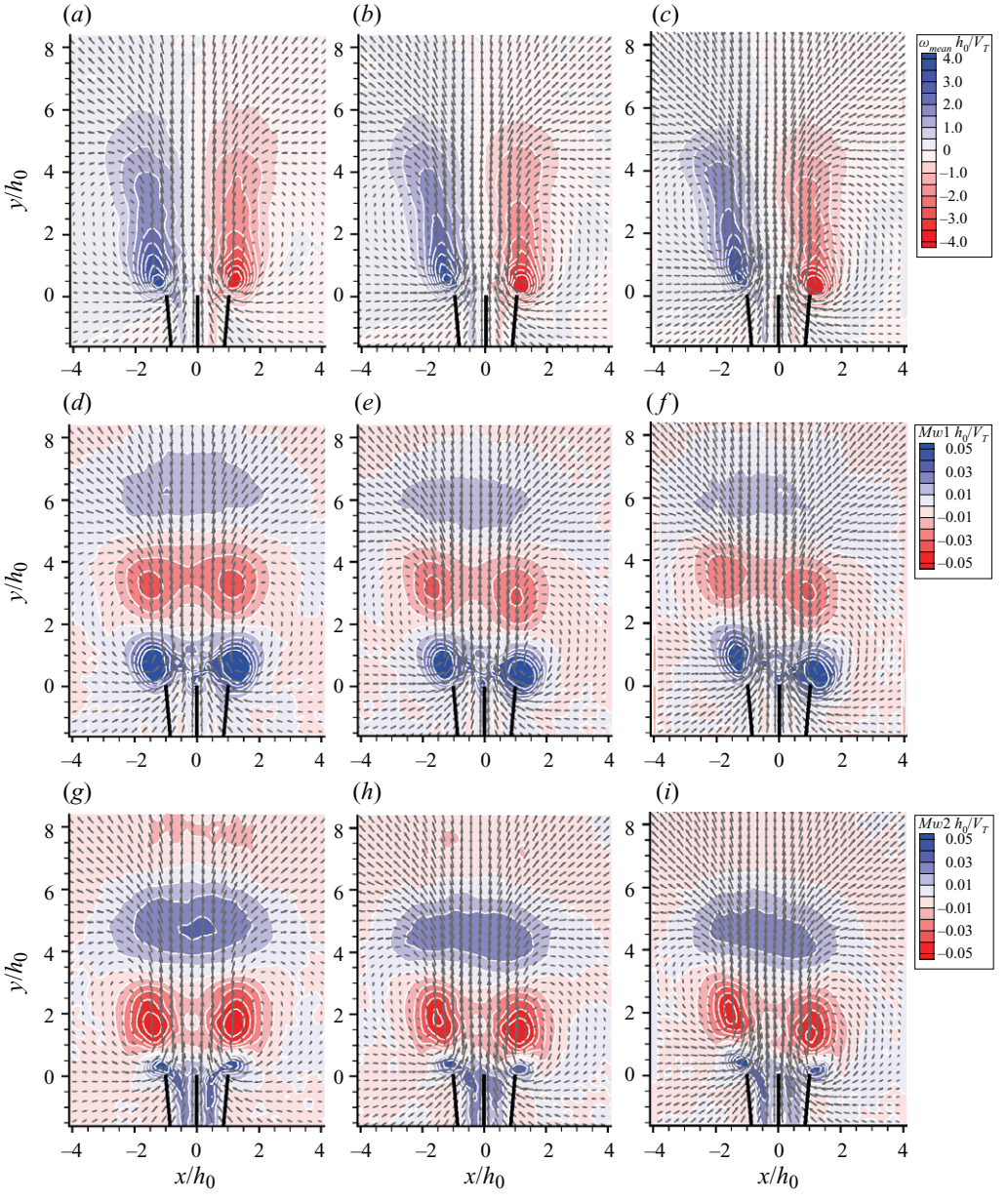


FIGURE 12. (Colour online) (*a–c*) Mean vorticity field, (*d–f*) POD mode 1 and (*g–i*) POD mode 2. The Reynolds number values are $Re_h = (a, d, g)$ 101, (b, e, h) 126 and (c, f, i) 146.

$x/h_0 = 0$. For the slightly inclined flows, $Re_h = 126$ and 146, clear asymmetric mode shapes are seen in the third and fourth modes. The fourth-mode shape is quite similar for $Re_h = 126$ and 146, but a clear difference is seen in the fourth mode of $Re_h = 101$.

3.4. *Three-dimensional effects in the mean trajectories*

The three-dimensionality of the flow was already mentioned by Kim *et al.* (2004). A complex secondary flow forms near the end plates to conserve mass. This flow can be observed by measurements taken at positions $b/z = 0.15$ and 0.30. In figure 14 the

https://doi.org/10.1017/S0022112010005318 Published online by Cambridge University Press

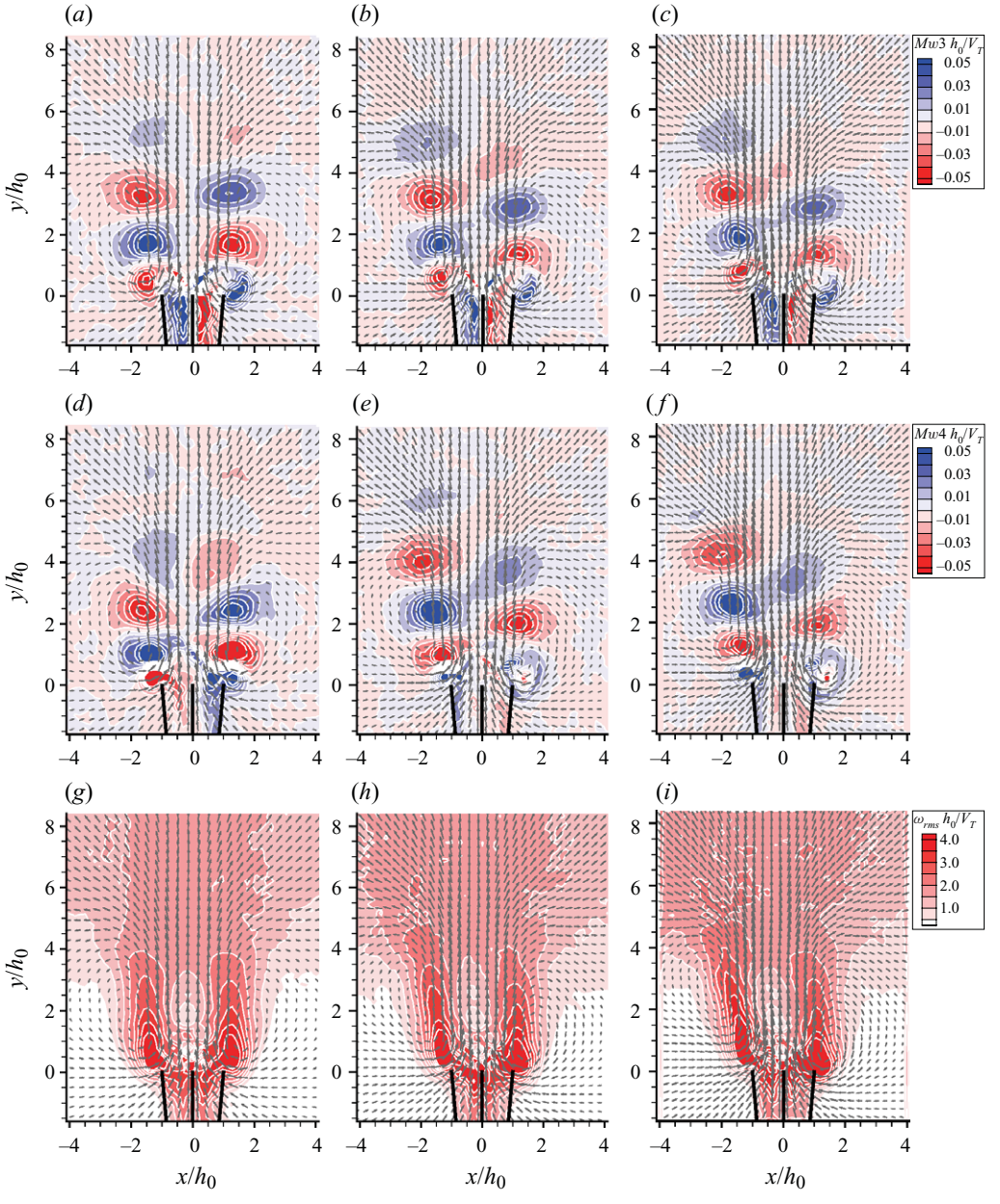


FIGURE 13. (Colour online) (*a–c*) POD mode 3, (*d–f*) POD mode 4 and (*g–i*) fluctuation of the vorticity. The Reynolds number values are $Re_h = (a, d, g)$ 101, (b, e, h) 126 and (c, f, i) 146.

averaged flow fields and vorticity, together with the averaged vortex centre locations, are given for $Re_h = 126$.

On the left side the velocity field and vorticity distribution form the aforementioned pseudo-jet. The closed symbols show the CCW vortex locations; the open ones show the CW vortex locations. In the centre plane ($z/b = 0$) the evolving vortices move along the shear layers, as highlighted by the vorticity distribution. Two large rolls are formed to feed the pseudo-jet from a region upstream of the cantilever

https://doi.org/10.1017/S0022112010005318 Published online by Cambridge University Press

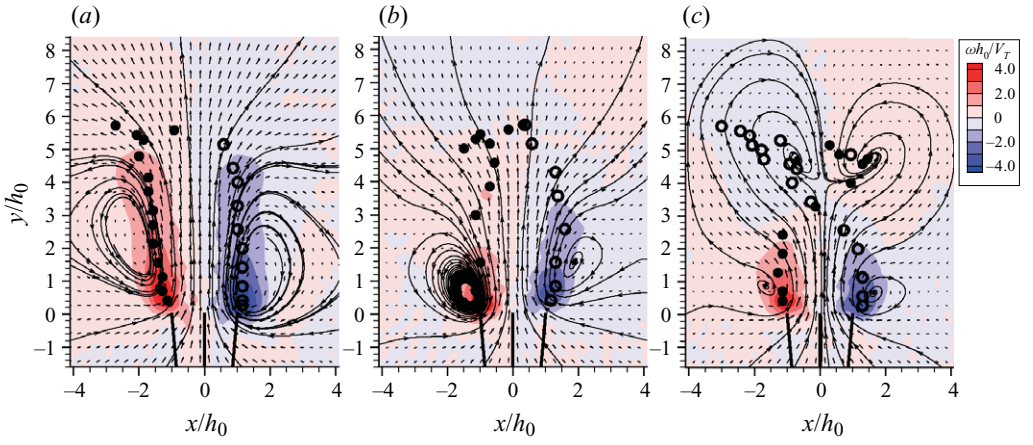


FIGURE 14. (Colour online) Average vorticity distribution and streamlines for different planes in the z-direction at $Re_h = 126$: $z/b = (a)\ 0$, $(b)\ 0.15$ and $(c)\ 0.3$. The vortex trajectories, given by the symbols, are overlaid and show clearly the three-dimensional effects. The filled symbols represent CCW vortices and the open symbols CW vortices.

tip. With increasing distance from the centre plane these two rolls become smaller. In the case of $z/b = 0.15$, the trajectories of the vortices seem to bend into the middle at around $x/h_0 = 0$ and $y/h_0 = 5$. This effect becomes much clearer for $b/z = 0.30$. The vortex trajectories even shift from one side to the other. They intersect at $x/h_0 = 0$ and $y/h_0 = 3$. The flow topology differs significantly from the one at the centre plane. In addition to the very small rolls that feed the pseudo-jet near ($y/h_0 = 1$), two rolls of the opposite sense of rotation can be observed at around $y/h_0 = 5$ with the vorticity distribution which changes sign at $y/h_0 \approx 3.5$. The two counter-rotating rolls generate reverse flow, which can also be confirmed in the flow measurement on the plane of $x/h_0 = 0$ as shown in figure 15. The boundary between the pseudo-jet and the reversed flow (top to bottom) coincides with the intersection points of the vortex trajectories $z/b = 0.15$ and $y/h_0 = 5$ and $z/b = 0.3$ and $y/h_0 = 3$. Because of the influence of the end plate at $z/b = 0.50$, the flow near the end plate is decelerated. This forces the vortices to move into the centre and further on, owing to their own sense of rotation. In that case the averaged trajectories show that the vortices from the left side move to the right side and vice versa. The magnitude of these vortices is lower than that close to the jet, but they are still recognizable as vortices. The vortex trajectories of the phase-averaged flow would hide this phenomenon.

4. Conclusion and outlook

The present study showed the flow characteristics induced by a vibrating cantilever plate, using a wavelet-based vortex analysis and the POD method. Phase-averaging often hides flow features for a vortex-dominant cyclic flow with one predominant frequency, since the fluctuations are smeared out. However, analysing individual vortex information such as the size, strength, distribution and position of each vortex, acquired by the wavelet analysis from phase-locked measurements, provides the detailed topology of the spatially fluctuating vortices at each step as well as the details of the flow generation process. The POD analysis provides an efficient method to describe the net effect of the flow without phase information. The general flow

https://doi.org/10.1017/S0022112010005318 Published online by Cambridge University Press

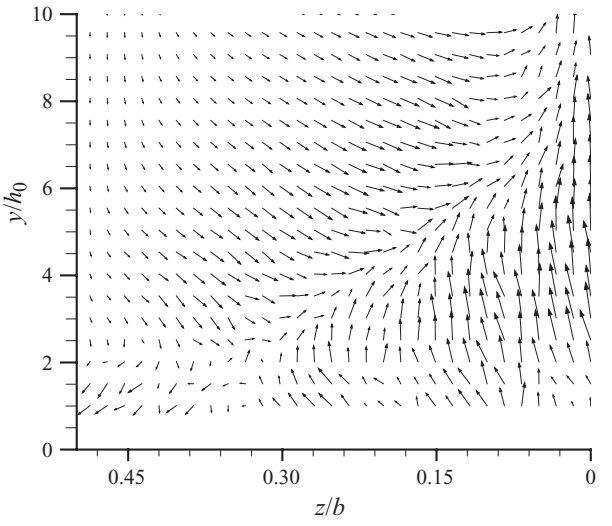


FIGURE 15. Spanwise flow measured on the plane of $x/h_0 = 0$ for $Re_h = 126$.

generation process of the cyclic flow is described well with mean flow and the first two POD modes. At higher modes clear differences are observed in the flows which are seen to be quite similar in the averaged flow fields.

A detailed numerical study with higher temporal resolution is needed to reveal all the different phenomena of the flow. The same methods as those presented here can be used to investigate the numerical data and will allow for comparison. Once the validity of the numerical model is proven, different parameters such as the cantilever length, frequency and chamber geometry can easily be simulated. Furthermore, the system can be optimized.

REFERENCES

ACIKALIN, T., RAMAN, A. & GARIMELLA, S. V. 2003 Two-dimensional streaming flows induced by resonating thin beams. *J. Acoust. Soc. Am.* **114**, 1785–1795.

ACIKALIN, T., WAIT, S. M., GARIMELLA, S. V. & RAMAN, A 2004 Experimental investigation of the thermal performance of piezoelectric fans. *Heat. Transfer Engng* **25**, 4–14.

ADRIAN, R. J. 1996 *Stochastic Estimation of the Structure of Turbulent Fields*, pp. 145–195. Springer.

BERKOOZ, G., HOLMES, P. J. & LUMLEY, J. L. 1993 The proper orthogonal decomposition in the analysis of turbulent flows. *Annu. Rev. Fluid Mech.* **25**, 539–575.

BERNERO, S. & FIEDLER, H. E. 2000 Application of particle image velocimetry and proper orthogonal decomposition to the study of a jet in counterflow. *Exp. Fluids* **29** (Suppl.), S274–S281.

BONNET, J. P., DELVILLE, J., GLAUSER, M. N., ANTONIA, R. A., BISSET, D. K., COLE, D. R., FIEDLER, H. E., GAREM, J. H., HILBERG, D., JEONG, J., KEVLAHAN, N. K. R., UKEILEY, L. S. & VINCENDEAU, E. 1998 Collaborative testing of eddy structure identification methods in free turbulent shear flows. *Exp. Fluids* **25**, 197–225.

BOURGUET, R. & BRAZA, M. 2007 Reduced order modeling for unsteady transonic flows around an airfoil. *Phys. Fluids* **19**, 111701.

BRAUD, C., HEITZ, D., BRAUD, P., ARROYO, G. & DELVILLE, J. 2004 Analysis of the wake-mixing-layer interaction using multiple plane PIV and 3D classical POD. *Exp. Fluids* **37**, 95–104.

BURMANN, P., RAMAN, A. & GARIMELLA, S. V. 2002 Dynamics and topology optimization of piezoelectric fans. *IEEE Trans. Compon. Packag. Manuf. Technol.* **25**, 592–600.

CIERPKA, C., WEIER, T. & GERBETH, G. 2008 Evolution of vortex structures in an electromagnetically excited separated flow. *Exp. Fluids* **45**, 943–953.

https://doi.org/10.1017/S0022112010005318 Published online by Cambridge University Press

Cordier, L. & Bergmann, M. 2003 Proper orthogonal decomposition, an overview. In *VKI LS 2003-03, Post-Processing of Experimental and Numerical Data* (ed. P. Millan & M.L. Riethmuller), pp. 1–45. Von Kármán Institute for Fluid Dynamics.

Delville, J., Ukeiley, L., Cordier, L., Bonnet, J. P. & Glauser, M. 1999 Examination of large-scale structures in a turbulent plane mixing layer. Part 1. Proper orthogonal decomposition. *J. Fluid Mech.* **391**, 91–122.

Farge, M. 1992 Wavelet transforms and their applications to turbulence. *Annu. Rev. Fluid Mech.* **24**, 395–457.

Hilberg, D., Lazi, W. & Fielder, H. E. 1994 The application of classical POD and snapshot POD in a turbulent shear layer with periodic structures. *Appl. Sci. Res.* **53**, 283–290.

Holmes, P. J., Lumley, J. L., Berkooz, G., Mattingly, J. C. & Wittenberg, R. W. 1997 Low-dimensional models of coherent structures in turbulence. *Phys. Rep.* **287** (4), 337–384.

Ihara, A. & Watanabe, H. 1994 On the flow around flexible plates, oscillating with large amplitude. *J. Fluids Struct.* **8**, 601–619.

Jeong, J. & Hussain, F. 1995 On the identification of a vortex. *J. Fluid Mech.* **285**, 69–94.

Kim, Y-H., Wereley, S. T. & Chun, C-H. 2004 Phase-resolved flow field produced by a vibrating cantilever plate between two endplates. *Phys. Fluids* **16**, 145–162.

Kimber, M. & Garimella, S. V. 2009 Measurement and prediction of the cooling characteristics of a generalized vibrating piezoelectric fan. *Intl J. Heat Mass Transfer* **52**, 4470–4478.

Kostas, J., Soria, J. & Chong, M. S. 2005 A comparison between snapshot POD analysis of PIV velocity and vorticity data. *Exp. Fluids* **38**, 146–160.

Lima, C. R., Vatanabe, S. L., Choi, A., Nakasone, P. H., Pires, R. F. & Silva, C. N. 2009 A biomimetic piezoelectric pump: Computational and experimental characterization. *Sensors Actuator* A **152**, 110118.

Linderman, R. J., Sett, S. & Bright, V. M. 2001 The resonant micro fan for fluidic transport, mixing and particle filtering. In *2001 ASME International Mechanical Engineering Congress and Exposition, New York.*

Lumley, J. L. 1967 The structure of inhomogeneous turbulent flows. In *Atmospheric Turbulence and Radio Wave Propagation* (2nd edn) (ed. A.M. Yaglom & V.I. Tatarski), pp. 166–178. Nauka, Moscow.

Raffel, M., Willert, C. E., Wereley, S. T. & Kompenhans, J. 2007 *Particle Image Velocimetry. A Practical Guide*. Springer.

Schram, C., Rambaud, P. & Riethmuller, M. L. 2004 Wavelet based eddy structure eduction from a backward facing step flow investigated using particle image velocimetry. *Exp. Fluids* **36**, 233–245.

Siegel, S., Cohen, K., Seidel, J. & McLaughlin, T. 2007 State estimation of transient flow fields using double proper orthogonal decomposition. *Notes Numer. Fluid Mech. Multidiscip. Des.* **95**, 105–118.

Sirovich, L. 1987 Turbulence and the dynamics of coherent structures. Part I. Coherent structures. *Q. Appl. Maths* **45**, 561–571.

Smith, T. R., Moehlis, J. & Holmes, P. J. 2005 Low-dimensional modeling of turbulence using the proper orthogonal decomposition: a tutorial. *Nonlinear Dyn.* **41**, 275–307.

Takato, K., Tsutsui, T., Akiyama, M. & Sugiyama, H. 1997 Numerical analysis of flow around a vibrating elastic plate. *Trans. JSME* B **64**, 194–202.

Tinney, C. E. & Jordan, P. 2008 The near pressure field of co-axial subsonic jets. *J. Fluid Mech.* **611**, 175–204.

Toda, M. 1979 Theory of air flow generation by a resonant type PVF2 Bimorph cantilever vibrator. *Ferroelectrics* **22**, 911–918.

Toda, M. 1981 Voltage-induced large amplitude bending device – PVF2 Bimorph – its properties and applications. *Ferroelectrics* **32**, 127–133.

Tsutsui, T., Akiyama, M., Sugiyama, H. & Shimanaka, K. 1996 Heat transfer enhancement around a rectangular cylinder set in near wake generated by elastically vibrating flat plate. *Trans. JSME* B **62**, 135–142.

Wait, S. M., Acikalin, T., Garimella, S. V. & Raman, A. 2004 Piezoelectric fans for the thermal management of electronics. Paper no. HMT-2004-C76. In *Proceedings of the 6th ISHMT/ASME Heat Mass Transfer Conference and 17th National Heat and Mass Transfer,*

https://doi.org/10.1017/S0022112010005318 Published online by Cambridge University Press

Kalpakkam, India (ed. Vaidyanathan, Prasad, Balaji & Joshi), pp. 447–452. New Delhi: Tata McGraw-Hill.

Wait, S. M., Basak, S., Garimella, S. V. & Raman, A. 2007 Piezoelectric fans using higher flexural modes for electronics cooling applications. *IEEE Trans. Compon. Packag. Manuf. Technol.* **30**, 119–128.

Watanabe, H., Ihara, A., Hirama, H. & Hayashizaki, S. 1990 Measurement of the three-dimensional flow field around an oscillating flat plate with LDV. *Trans. JSME* B **56** (532), 122–129.

Weier, T., Cierpka, C. & Gerbeth, G. 2008 Coherent structure eduction from PIV data of an electromagnetically forced separated flow. *J. Fluids Struct.* **24**, 1339–1348.

Wereley, S. T. & Gui, L. 2003 A correlation-based central difference image correction (CDIC) method and application in a four-roll mill flow PIV measurement. *Exp. Fluids* **34**, 42–51.

Yoo, J. H., Hong, J. I. & Cao, W. 2000 Piezoelectric ceramic Bimorph coupled to thin metal plate as cooling fan for electronic devices. *Sensors Actuators* A **79**, 8–12.

https://doi.org/10.1017/S0022112010005318 Published online by Cambridge University Press